Optics and Lasers in Engineering 49 (2011) 490–497

Contents lists available at ScienceDirect

Optics and Lasers in Engineering

journal homepage: www.elsevier.com/locate/optlaseng

Laser remelting of Al–1.5 wt%Fe alloy surfaces: Numerical and experimental analyses

Felipe Bertelli [a], Elisangela S. Meza [b], Pedro R. Goulart [c], Noé Cheung [d], Rudimar Riva [e], Amauri Garcia [a,*]

[a] Department of Materials Engineering, University of Campinas – UNICAMP, PO Box 6122, 13083-860 Campinas, SP, Brazil
[b] Department of Mathematics and Statistics, State University of Ponta Grossa, UEPG, 84030-900 Ponta Grossa, PR, Brazil
[c] Federal Institute of Education, Science and Technology of São Paulo – IFSP, 18202-000 Itapetininga, SP, Brazil
[d] Federal Institute of Education, Science and Technology of São Paulo – IFSP, 13872-551 São João da Boa Vista, SP, Brazil
[e] Institute for Advanced Studies, General Command for Aerospace Technology, PO Box 6044, 12228-970 São José dos Campos, SP, Brazil

ARTICLE INFO

Article history:
Received 10 October 2010
Received in revised form
6 December 2010
Accepted 4 January 2011

Keywords:
Laser
Melting
Microstructure refinement
Al–Fe alloy

ABSTRACT

A 3D heat transfer mathematical model based on the finite element method is applied to the laser surface remelting (LSR) process with a view to simulating temperature fields and melt pool dimensions. The theoretical predictions furnished by the model are validated against LSR experimental results from tests carried out in the present study with Al–1.5 wt%Fe alloy samples. The work also encompasses an analysis of microstructural and microhardness variations throughout the resulting treated and untreated zones. A remarkable effect of the LSR treatment on the mechanical and corrosion resistance of the treated samples is shown.

1. Introduction

Laser surface treatments are efficient means of local transformation of mechanical and chemical properties. The cleanliness, the speed and the automation inherent to the laser process are also factors in making laser applications extremely competitive in an industrial environment [1,2]. The laser surface remelting (LSR) process is accomplished by rapidly traversing a continuous, high energy-density laser beam over the material to produce a thin molten layer at the material surface. The ability to maintain a cold substrate while melting a thin surface layer results in rapid quenching of the molten region once the energy source is removed, resulting in very high solidification cooling rates (from 10^5 to 10^8 K s^{-1}) [3]. LSR has been shown to be capable of producing a wide variety of novel and interesting surface microstructures and properties [4–7].

The interactions between a laser beam and an alloy surface is controlled by a number of variables. A particular combination of power density and interaction time defines a specific operational regime within the spectrum of operating conditions, which results in the occurrence of a unique materials processing effect. Moreover, due to the reduced size of the treated zone, physical measurements of important parameters such as the temperature and velocity fields in the melt pools are not easy tasks. Therefore, mathematical modeling of LSR processes can enhance both qualitative and quantitative understanding of the process mechanics that cannot be obtained otherwise. A number of studies existing in the literature examine the interaction between the laser energy and the substrate and the corresponding phase change in the irradiated region during surface treatments. Cheung et al. [8] examined the laser surface remelting of an aluminum alloy by a mathematical heat transfer model based on the finite difference method, which takes into account convection effects applying an effective thermal conductivity approach. Yilbas et al. [9] analyzed laser heating of a cemented carbide tool and computed the corresponding temperature distribution in the irradiated region using a melting/solidification process based on an enthalpy-porosity technique. Krishna et al. [10] investigated heat and momentum transfer in a laser alloying process by modeling the phase change using a fixed-grid, enthalpy-porosity technique and considering natural convection in the melt. Raj et al. [11] developed a three-dimensional transient model to analyze heat transfer, fluid flow and mass transfer during a laser alloying process, solving the coupled momentum, energy and species equations by a finite volume procedure. Shen et al. [12] developed an analytical model permitting the problem of laser heating and melting to be analyzed. The temperature profile before and after melting can be described by the solution, as well as the depth of the molten zone as a function of the laser power density.

* Corresponding author. Tel.: +55 19 35213320; fax: +55 19 32893722.
E-mail address: amaurig@fem.unicamp.br (A. Garcia).

0143-8166/
doi:10.1016/j.optlaseng.2011.01.007

Aluminum–iron alloys are of considerable commercial interest, partly because iron is almost invariably present at significant levels (0.2–1.0 wt%). Iron is added intentionally in some alloys to increase the high-temperature strength. Under equilibrium solidification conditions, any iron in excess of its solid solubility limit (0.04 wt%Fe) forms a eutectic constituted by an Al-rich primary phase and intermetallic Al_3Fe particles. However, during non-equilibrium solidification typical of DC castings considerably different cooling rate exists at the ingot surface and at the center, causing the formation of metastable Al_mFe and Al_6Fe intermetallic phases in addition to the stable Al_3Fe phase [13]. Gremaud et al. [14] reported that under rapid solidification conditions (LSR process) of Al–Fe alloys cellular-dendritic structures, banded structures and supersaturated solid solutions can be observed. Allen et al. [13] and Griger et al. [15] have studied the formation of Al_3Fe and Al_6Fe intermetallic particles as a function of both the cooling rate and the chemical composition of Al–Fe alloys. A recent study using a water-cooled directional solidification apparatus has shown that the Al_6Fe phase prevails for growth rates and cooling rates higher than 0.7 mm s^{-1} and 1.5 K s^{-1}, respectively [16]. A further study demonstrated that the tensile strength increases with increase in alloy Fe content and with a more homogeneous distribution of intermetallic Al_6Fe fibers. For coarser microstructural cellular arrangements, the Al_6Fe fibers remain more concentrated in the intercellular regions provoking a deleterious effect on the mechanical properties due to the brittle nature of these fibers [17].

The present study focuses on the application of a three-dimensional numerical approach in order to simulate the laser surface remelting of an Al–1.5 wt%Fe alloy surface. An experimental analysis is carried out with a view to validating the model predictions. The work also deals with the correlation of laser process parameters and the dimension of the treated zone, the characterization of microstructural parameters by optical and scanning electron microscopy (SEM), and hardness variations throughout the laser treated and unmolten zones.

2. Numerical analysis

The temperature fields and the evolution of the laser remelting process are investigated by means of a finite element method. In order to accurately determine the temperature fields, a 3-D finite element model is developed. The mathematical model is based on the general heat conduction equation [18], which is given in matricial form by

$$\rho c\left(\frac{\partial T}{\partial t}+\{v\}^T\{\nabla\}T\right)+\{\nabla\}^T\{q\}=\ddot{q} \tag{1}$$

where ρ is the density, c the specific heat, T the time-dependent local temperature, $\{\nabla\}$ the vector operator $\{\partial/\partial X,\partial/\partial Y,\partial/\partial Z\}$, $\{v\}$ the velocity vector for mass transport of heat $\{V_x,V_y,V_z\}$, and $\ddot{q}$ the heat generation rate per unit volume, $\{q\}$ the heat flux vector, and the Fourier's law is used to relate $\{q\}$ to the thermal gradient:

$$\{q\}=[D]\{\nabla\}T \tag{2}$$

where the conductivity matrix $[D]$ is given by

$$[D]=\begin{bmatrix} k_x & 0 & 0 \\ 0 & k_y & 0 \\ 0 & 0 & k_z \end{bmatrix} \tag{3}$$

k_x, k_y and k_z=effective thermal conductivity k_{eff} if the nodal temperature is above the fusion temperature.

Substituting Eq. (2) into Eq. (1) and letting $\{V\}=0$ because the effect of liquid metal convection is taken into account by using the effective thermal conductivity approach [8], the governing equation for the temperature field is given by

$$\rho c\frac{\partial T}{\partial t}=\{\nabla\}^T(D\{\nabla\}T)+\ddot{q} \tag{4}$$

As the laser treatment includes the surface remelting, the latent heat of fusion has to be taken into account by the finite element calculation. In the present approach, the total latent heat is incorporated, as follows:

$$\ddot{q}=-\rho L\frac{\partial f_L}{\partial t} \tag{5}$$

where the minus sign means that the energy must be absorbed due to solid/liquid phase transformation, L is the latent heat and f_L is the liquid fraction.

The enthalpy is defined as

$$H=\int \rho c dT+\rho L_H f_L \tag{6}$$

The variation of enthalpy in time is obtained by deriving Eq. (6):

$$\frac{\partial H}{\partial t}=\rho c\frac{\partial T}{\partial t}+\rho L\frac{\partial f_L}{\partial t} \tag{7}$$

and hence, Eq. (4) can be re-written in terms of enthalpy:

$$\frac{\partial H}{\partial t}=\{\nabla\}^T(D\{\nabla\}T) \tag{8}$$

The following assumptions were also adopted in deriving the model:

(1) the laser beam is of Gaussian type in a continuous mode,
(2) the sample moves at a constant relative velocity,
(3) the material is isotropic and opaque with constant thermal and optical properties,
(4) heat losses by convection and radiation to the environment are negligible as compared with the heat intensity provided by the incident beam,
(5) considering that only a part of the top surface is remelted by the laser beam, it is assumed that the sample is semi-infinite, thus no heat exchange from the side and bottom sample surfaces to the environment is considered. When the whole top surface is treated, convective and radiative boundary conditions must be assumed at the remaining surfaces.

The intensity of the heat flux applied on the top surface can be calculated from the applied Gaussian beam intensity profile over the beam spot area. The Gaussian model assumes that the laser irradiance is symmetric with respect to its propagation direction and the maximum heat input I_o (W m^{-2}) is located at the center of the beam. The beam radiation at any point is defined as [19]

$$I=AI_o e^{-2r^2/r_0^2} \tag{9}$$

where r_0 is the beam radius corresponding to the point where the irradiance is reduced to $1/e^2$, r is the radial distance from the center and A is the laser energy absorptivity of a material, which is known to depend on a number of factors such as the surface finishing, level of surface oxidation and laser wavelength [20]. The absorptivity used in this work was adopted as the same as pure aluminum, reported by Ujihara [21], considering that the small solute content of the alloy (1.5 wt%Fe) do not cause considerable changes in the absorptivity behavior.

The laser beam energy is absorbed by the surface of the material and transmitted by heat conduction to the inner part of the sample:

$$k\frac{\partial T}{\partial z}\bigg|_{surf}=I \tag{10}$$

The solution was generated in two steps. First the position of the heat source model was modified according to the beam speed, and then a transient heat transfer analysis with phase transformation was performed. An appropriate time step scheme was used to achieve fast convergence of the solution and reasonable accuracy. The 3-D finite element mesh performed by a finite element analysis code (ANSYS Inc., Southpointe, PA, USA) is shown in Fig. 1. In the area subjected to the laser treatment, a dense mesh of cubic elements was used, as shown in Fig. 1, and a coarse mesh of tetrahedral elements was adopted for the rest of the sample.

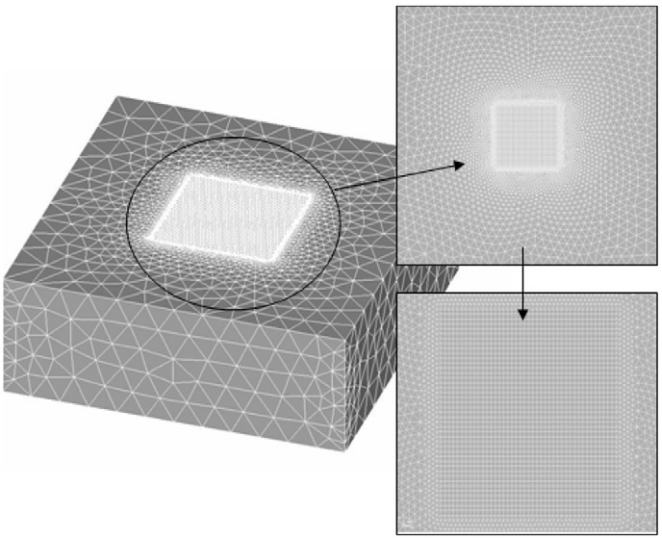

Fig. 1. Finite element mesh.

3. Experimental procedure

Commercially pure grade (c.p.) Al (99.76 wt%) and Fe (99.97 wt%) were used to prepare the Al–1.5 wt%Fe alloy. The mean impurities detected were: Fe (0.09 wt%), Si (0.06 wt%), Cu (0.06 wt%), Ni (0.03 wt%) and Si (0.01 wt%), Cu (0.01 wt%), Ni(0.01 wt%), besides other elements found with concentrations less than 50 ppm. The Si content is lower than 0.15 wt%Si, which has been reported as the limiting Si content permitting to avoid AlFeSi to be the dominant intermetallic phase [22]. A directional solidification apparatus was used to obtain an Al–1.5 wt%Fe alloy cylindrical casting. Specific information about this experimental set-up can be found in a previous article [23]. The cylindrical ingots were subsequently sectioned along its vertical axis, ground and etched with an acid solution (Poulton's reagent: 5 mL H_2O; 5 mL HF – 48%; 30 mL HNO_3; 60 mL HCl) to reveal the columnar macrostructure. A longitudinal sample, coincident with the columnar growth direction, was extracted to be used in the laser remelting experiments, as shown in Fig. 2.

Table 1
Thermophysical properties used in simulations [21,23].

Properties	Symbol/unit	Al–1.5 wt.%Fe
Thermal conductivity	k_S (W m^{-1} K^{-1})	219.2
	k_L	91.2
Specific heat	c_S (J kg^{-1} K^{-1})	1247
	c_L	1166
Density	ρ_S (kg m^{-3})	2620
	ρ_L	2450
Latent heat of fusion	L (J kg^{-1})	387,000
Liquidus temperature	T_{Liq} (°C)	653.4
Absorptivity	A (%)	37

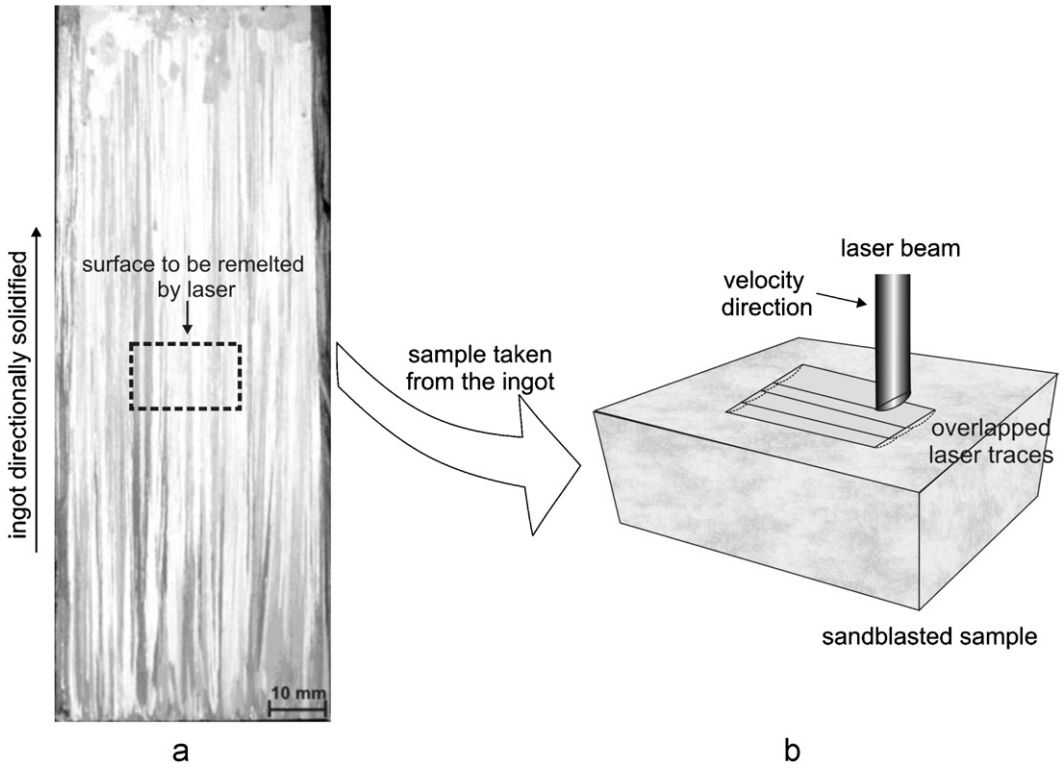

Fig. 2. (a) Macrostructure of the directionally solidified Al–1.5 wt%Fe alloy ingot and region from where the sample to be laser treated was extracted. (b) Schematics of the sample subjected to the LSR treatment.

The laser equipment used in the surface treatment experiments was an Ytterbium fiber laser (IPG, YLR 2000S), which emits radiation at a wavelength of 1070 nm and has a maximum power of 2000 W. The focused beam diameter was about 100 μm. The laser head is integrated with a CNC driven XYZ table where the sample is placed and moved for treatment. The following operational conditions were used during the laser surface remelting experiments: laser average power of 600 W; laser beam speeds from 40 to 80 mm s^{-1} and the laser beam was defocused 3 mm to permit a beam spot diameter of 0.3 mm to be achieved. It was observed that these parameters did not allow phase change from liquid to vapor, avoiding material losses. Before laser treatments, the sample surface was sandblasted in order to enhance energy absorption from the laser beam.

Selected transverse (perpendicular to the growth direction) sections of the laser trace were prepared by conventional metallographic techniques. These sections were etched with a solution of 0.5% HF in distilled water and were subsequently analyzed by a scanning electron microscope (SEM). Image processing systems Neophot 32 (Carl Zeiss, Esslingen, Germany) and Leica Quantimet 500 MC (Leica Imaging systems Ltd., Cambridge, England) were used to measure cellular and interphase spacings, λ.

Based on the method for quantitative analysis of intermetallics of aluminum alloys proposed by Simensen et al. [24], a glass apparatus [16] was used to dissolve the Al-rich matrix and the eutectic aluminum-phase so that only Al–Fe intermetallic particles remained. The samples of about 3–5 g were partially dissolved in distilled 1-butanol under argon atmosphere. After dissolution, the butanol and the aluminum butoxides were conducted through a Teflon filter with a pore size of 0.45 μm. The undissolved intermetallics retained by the Teflon filter were identified and analyzed by X-ray diffraction and scanning electron

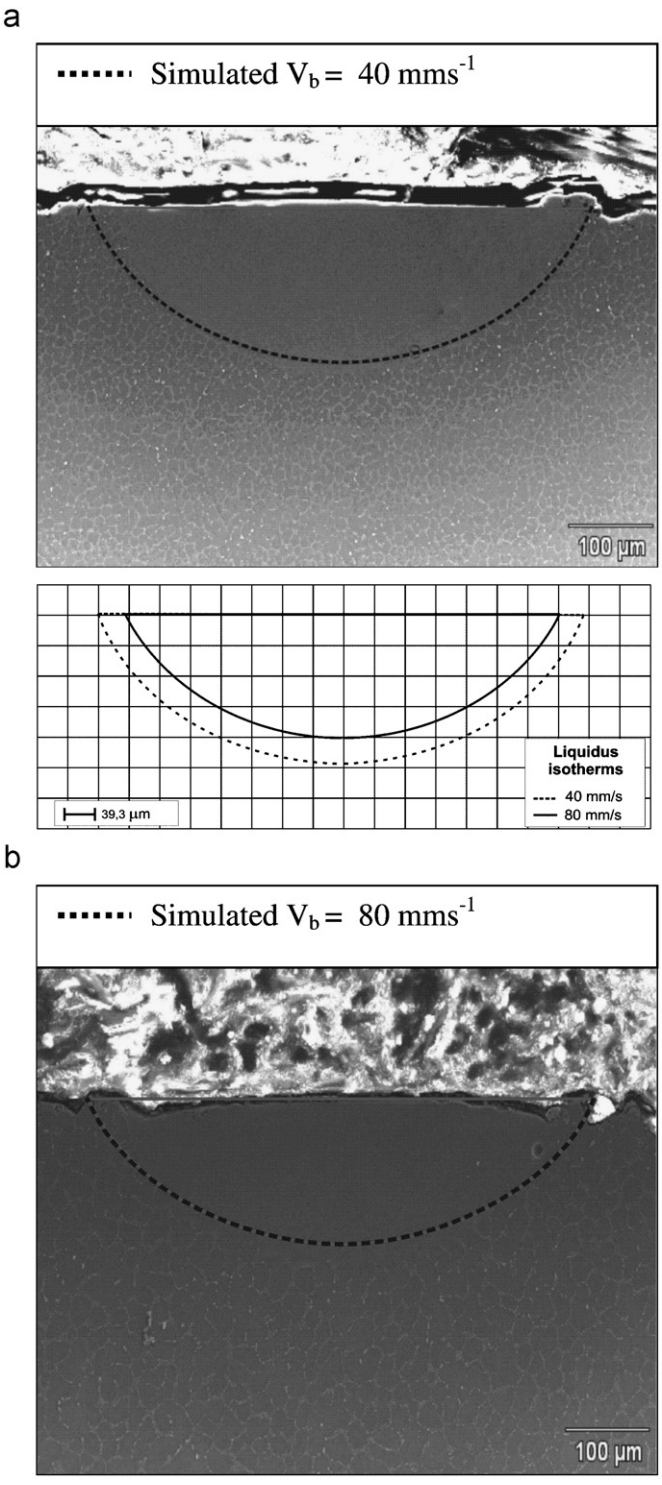

Fig. 3. Simulated and experimental pool profiles for laser beam rates of (a) 40 mm s^{-1} and (b) 80 mm s^{-1}.

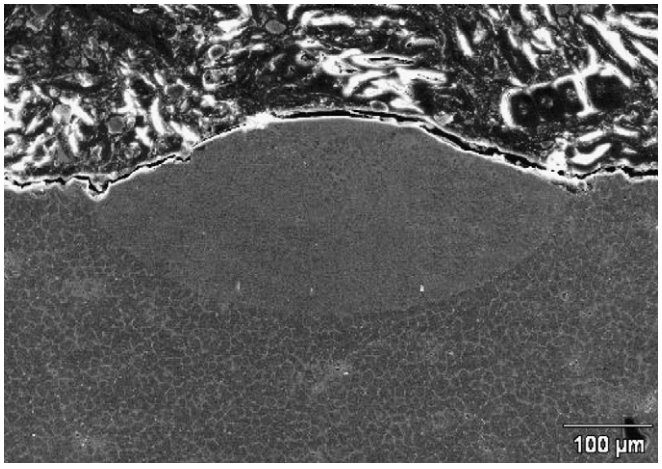

Fig. 4. Experimental pool profile for a laser beam rate of 20 mm s^{-1}.

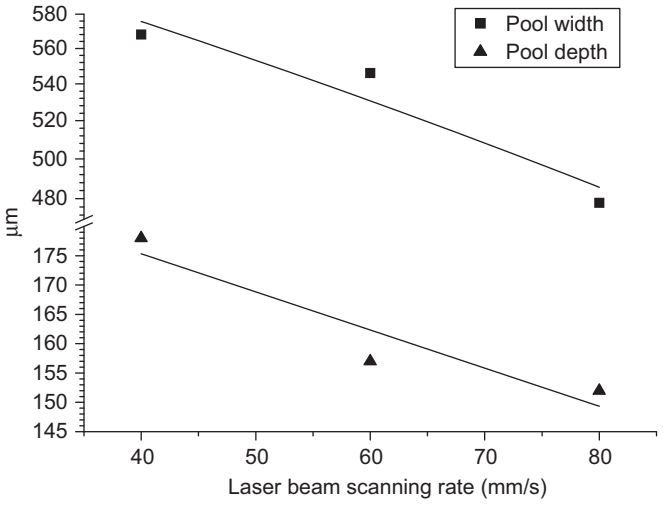

Fig. 5. Experimental evolution of the depth and width of single laser traces as a function of beam rate.

microscopy (SEM) with energy-dispersive X-ray analyzer. In order to achieve a better visualization of the SEM microstructures, the samples were ever rotated in about 30°.

The extracted intermetallics obtained from the solidified samples were characterized by XRD with a Rigaku DMAX 2200 diffractometer (40 kV, 30 mA), in Bragg–Brentano reflection geometry with Cu Kα radiation ($\lambda = 1.5418$ Å). The data were obtained between 10° and 70° 2θ in steps of 0.1° with counting time of 3 s.

Vickers microhardness tests were performed on the samples cross sections by using a test load of 10 g for the treated zone and 100 g for the untreated zone. The purpose of the microhardness tests was to document the variation of strength along the different microstructural zones induced by the LSR treatment.

4. Results and discussion

In order to determine the effects of process parameters on the melting and rapid cooling phases typical of the laser treatment, the finite element approach detailed in Section 2 was applied to the

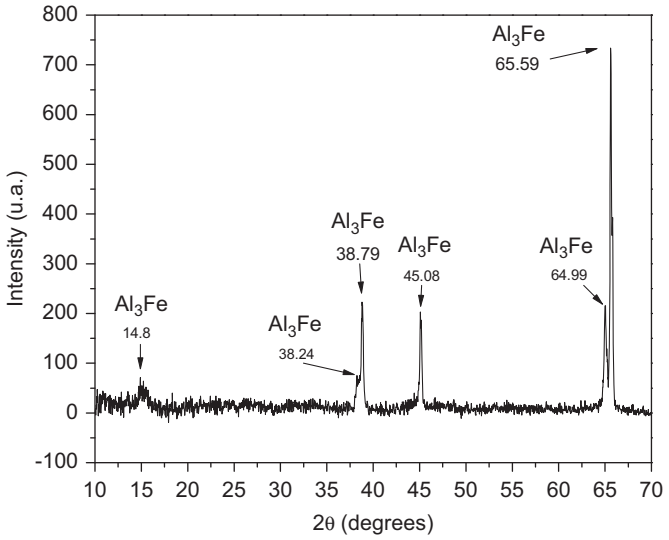

Fig. 7. X-ray diffractogram of the LSR treated region of the Al–1.5 wt%Fe alloy sample.

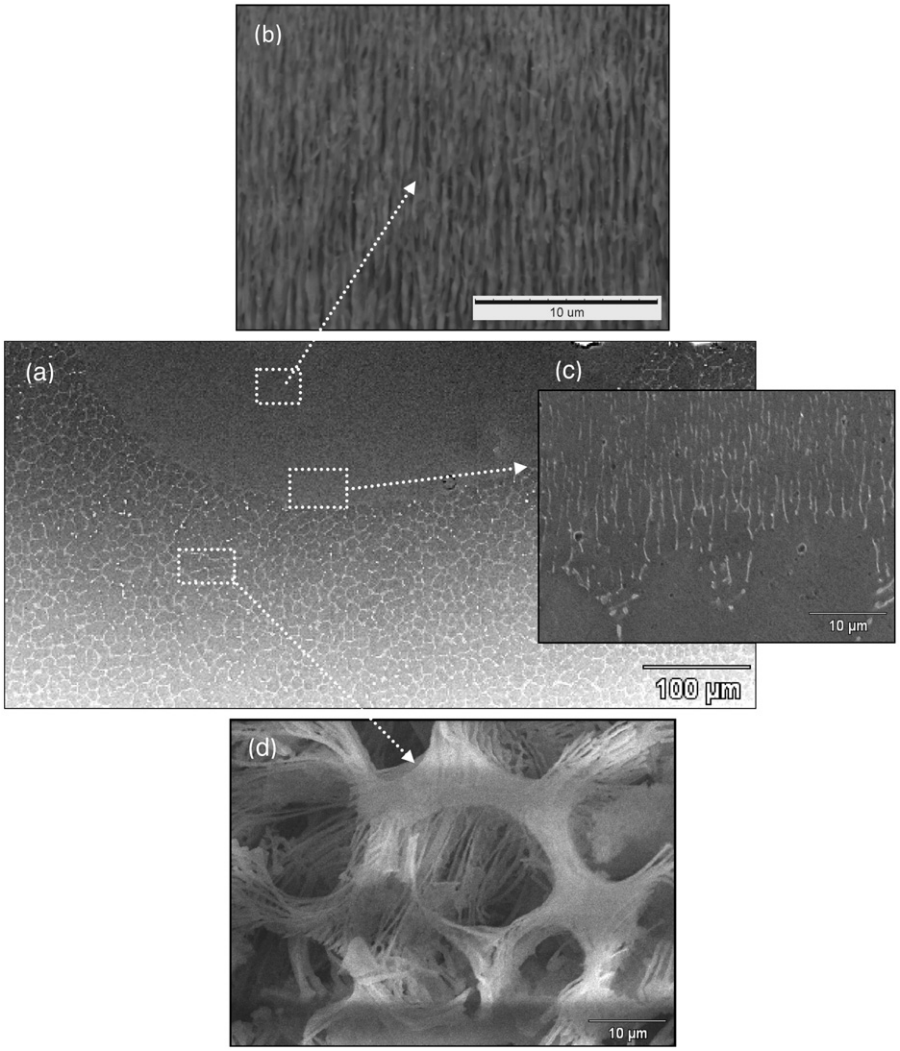

Fig. 6. (a) Microstructure of the cross section of the laser treated sample showing the remelted region and the substrate; (b) laser treated microstructure after the dissolution of the Al-rich matrix with butanol for 20 min; (c) substrate/resolidified layer interface; and (d) substrate after the dissolution of the Al-rich matrix with butanol for 20 min evidencing the resulting network of Al_6Fe fibers.

heating and transient cooling processes. Using this method, the width and length of the melt pool can be calculated as a function of the laser power and beam rate (V_b). The laser surface remelting (LSR) simulations were performed considering the thermophysical properties listed in Table 1 [21,23], the experimental laser power of 600 W and V_b from 20 to 80 mm s^{-1}. A comparison between experimental and simulated pool profiles are shown in Fig. 3 for beam rates of 40 and 80 mm s^{-1}, and a good agreement between theoretical and experimental profiles can be observed. At beam rates lower than 30 mm s^{-1}, the molten pool loses its steady-state regular form which is thought to be caused by oscillatory convective currents in the liquid and Marangoni effects [25], as can be seen by the bulging at the top of the laser track which resulted from a LSR treatment at a beam rate of 20 mm s^{-1}, shown in Fig. 4.

Fig. 5 shows the evolution of the laser pool dimensions, i.e., the experimental depth and width of single laser traces as a function of the beam rate. The evolution of both the laser trace depth and width was found to be linear with beam rate, decreasing with increasing V_b due to the lower interaction time between the power source and the sample. Zhu et al. [26] also reported a stable linear evolution between the depth of the molten zone and the beam rate within a range from 27 to 50 mm s^{-1} during laser melting of a Zn–Al alloy.

In addition to promoting higher melting efficiencies, the reduction in thermal conduction to the substrate also leads to increased temperature gradients and thus increases the cooling rates during resolidification of the melt pool. During the LSR process, after the cessation of energy input in a specific section, melting continues, however briefly, before the onset of solidification. Thus, the cooling rate and the solidification velocity at the bottom of the pool are both initially close to zero. The cooling rate starts at zero and tends to be a constant value as solidification proceeds to the pool surface. On the other hand, the solidification velocity varies markedly over the pool depth, from zero at the interface with the substrate up to a maximum at the surface which can approach the magnitude of V_b towards the surface of the melt pool [14]. The microstructural evolution along the laser treated region will depend on these solidification thermal parameters.

Fig. 6 depicts the microstructural features of the treated zone and substrate, which was originally directionally solidified in a water-cooled mold. A cellular microstructure prevailed in the substrate and a eutectic mixture formed by the Al-rich phase and an Al–Fe intermetallic characterizes the resolidified layer. The remarkable change in the microstructure scale at the interface can be seen in Fig. 6c. No evidence of cellular/dendritic transition was found and the cellular spacing varied from an average value of 13 μm in the non-treated zone to an interphase spacing of about 1.4 μm in the resolidified zone, i.e., a decrease of about 10 times. The dissolution of the Al-rich matrix in the substrate, using the technique described in the experimental section, permitted a clear visualization of the network of interconnected intermetallic fibers located in the intercellular region, as shown in Fig. 6d. As previously reported [16], for an Al–1.5 wt%Fe alloy solidified at cooling rates typical of cooled molds the metastable Al–Al_6Fe eutectic prevails, which was confirmed by X-ray diffraction analysis.

Fig. 6b shows a typical microstructure of the treated region after dissolution of the Al-rich matrix with a view to emphasizing the intermetallic particles. These particles seem to have a plate-like character instead of rod-like fiber morphology as those of the Al_6Fe fibers shown in Fig. 6d. It is generally accepted that with increasing solidification velocities the Al_3Fe equilibrium phase is first replaced by the metastable Al_6Fe and at a high velocity regime by Al_mFe ($m \sim 3.96$) [15]. Gilgien et al. [25] carried out LSR experiments with an Al–Fe alloy ($V_b = 10$ mm s^{-1}) and reported that, except for a dendritic α-Al microstructure at the top of the laser trace the resolidified layer was formed by an Al–Al_6Fe eutectic, which follows the growth direction. In the present study no evidence of dendritic microstructure has been found. As shown in Fig. 6b the eutectic structure is also aligned with the growth direction, but the platelet intermetallic (light areas) was shown to

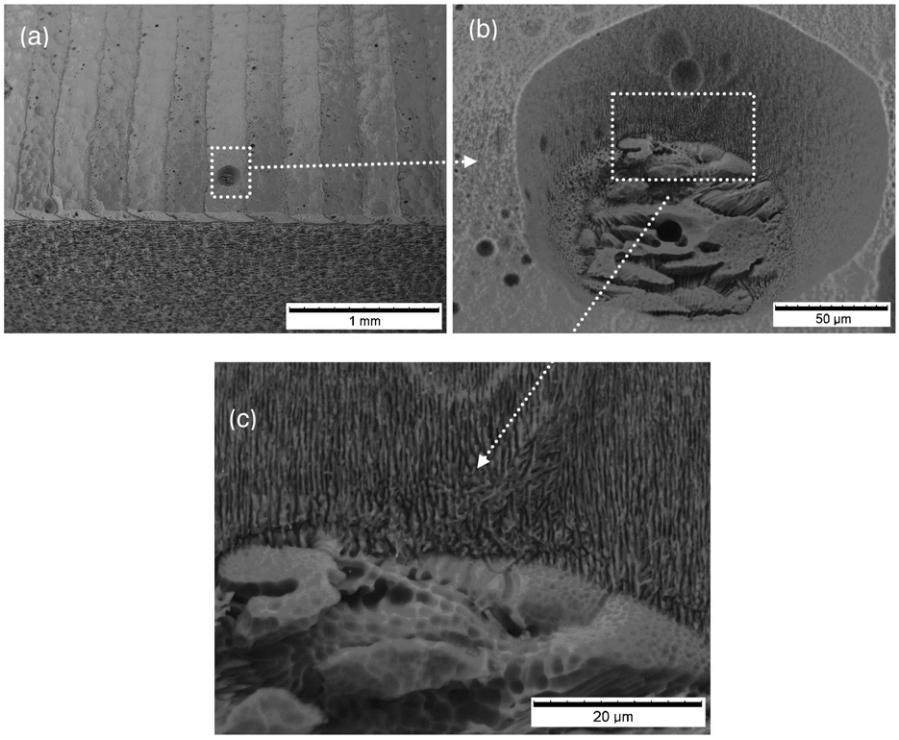

Fig. 8. (a) Selected pore in a particular laser trace; (b) region close to the resolidified layer/substrate interface etched with a Keller reagent; and (c) visualization of differences in the microstructure scale.

be Al_3Fe according to the X-ray diffractogram of Fig. 7. It is often considered that at high cooling rates, due to kinetic restrictions there is not enough time for the atoms to arrange themselves in a stable structure [27]. However, the development of solidification microstructures along the LSR process has some particular characteristics. The liquid pool, which is created during heating, is contained by its own solid, i.e., during the cooling stage no nucleation is involved and an epitaxial solidification occurs. Moreover, the onset of solidification at the molten pool/substrate interface is characterized by a solidification velocity that approaches zero [14], favoring the initial formation of the stable Al–Al_3Fe eutectic. This structure probably continues to grow in spite of the sudden increase in the solidification velocity over the pool depth, i.e., the equilibrium Fe aluminide is not displaced with increasing solidification velocity by a metastable aluminide. This could explain the present experimental evidence. Fig. 8 shows details of the microstructural transition between the resolidified layer and the substrate observed inside a pore which was etched with a Keller reagent.

A remarkable effect of the LSR treatment on hardness of the treated region of the Al–1.5 wt%Fe alloy sample can be noted. The hardness increased from 32 HV in the substrate to 58 HV in the remelted region. The higher hardness value of the remelted region is mainly due to the fineness of the eutectic mixture and the corresponding homogeneous distribution of intermetallic particles, which resulted from the laser treatment. The increase in hardness in laser surface processing is not just due to microstructural refinement and homogenization and formation of metastable phases. The surface hardness is also intrinsically coupled with a change in the internal stress distribution. For instance, during laser surface modification of steels a martensitic transformation in the heated surface layer causes compressive stresses at the surface and tensile stresses in the heat affected zone. Depending on the degree of austenitization and subsequent martensitic transformation, laser processing can generate different internal stresses distribution. As pointed out by Krishna and Bondyopadhyay [28], the high strength of austenite due to solid solution strengthening and possible presence of residual stresses can decrease the temperature of martensitic transformation thus leading to higher retained austenite.

The technique used to dissolve the Al-rich matrix with butanol, described in the experimental section, has also permitted

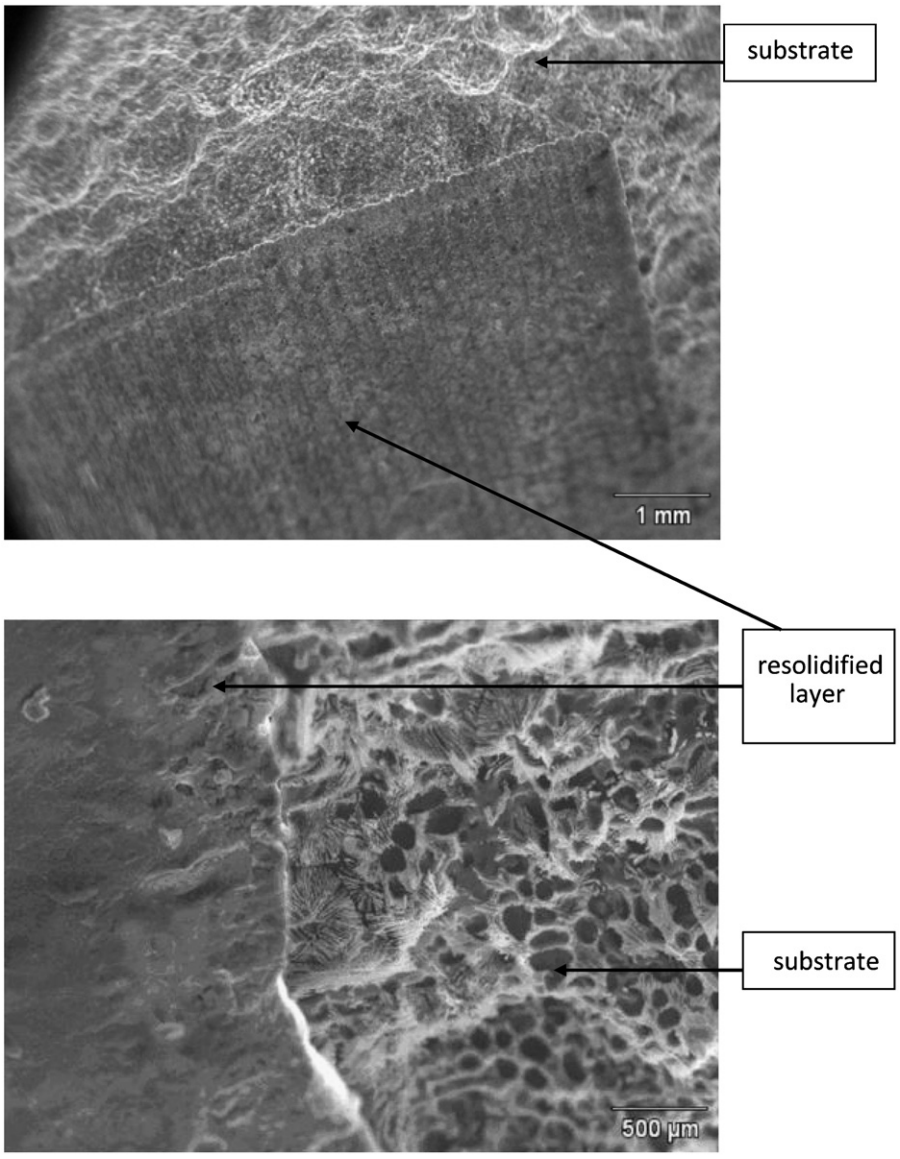

Fig. 9. Corroded surfaces of substrate and treated surface of the Al–1.5 wt%Fe alloy sample after the dissolution of the Al-rich matrix with butanol.

to support the significant increase in the corrosion resistance experienced by the laser resolidified layer, compared with that of the substrate, as shown by the corresponding micrograph in Fig. 9. A recent study [29] has shown that for quasi-eutectic Al–Fe compositions a more extensive distribution of the intermetallic particles, which is associated with higher cooling rates during solidification, provides a protective effect with the nobler intermetallic particles enveloping the Al-rich phase in the eutectic mixture, thus providing a better corrosion resistance.

5. Conclusion

A transient three-dimensional heat transfer numerical approach applied to the laser surface remelting process and based on a finite element method has been developed permitting to predict temperature distributions and dimensions of the melt pool. The LSR experimental analysis carried out with Al–1.5 wt%Fe alloy samples has revealed different microstructural zones in the laser trace cross section: a cellular microstructure in the substrate having a metastable Al–Al_6Fe eutectic in the intercellular region and the resolidified layer being formed by a stable Al–Al_3Fe eutectic aligned with the growth direction. No evidence of cellular/dendritic transition was found and the cellular spacing varied from an average value of 13 μm in the substrate to an interphase spacing of about 1.4 μm in the resolidified layer, i.e., a decrease of about 10 times. Vickers microhardness tests carried out along the sample cross sections have shown an increase on hardness of the treated region of about 1.8 × if compared with that of the original substrate. Mechanical properties of both the substrate and resolidified layer have been estimated by experimental equations based on the scale of microstructure parameters confirming the effectiveness of the laser treatment in the improvement of surface mechanical properties. A microstructural analysis performed after the dissolution of the Al-rich matrix with butanol on both treated and substrate regions gave indications of a significant increase in the corrosion resistance after the LSR process.

Acknowledgments

The authors acknowledge the financial support provided by FAPESP (The Scientific Research Foundation of the State of São Paulo), FAEPEX-UNICAMP and CNPq (The Brazilian Research Council). The authors also thank IEAv (Institute for Advanced Studies), Sao José dos Campos – SP, for permitting the use of laboratory facilities.

References

[1] Steen PH, Ehrhard P, Schüssler A. Depth of melt-pool and heat-affected zone in laser surface treatments. Metall Mater Trans 1994;22A:427–35.
[2] Cheung N, Ierardi MCF, Garcia A, Vilar R. The use of artificial intelligence for the optimization of a laser transformation hardening process. Lasers Eng 2000;10:275–91.
[3] Kurz W, Fisher DJ. Fundamentals of solidification. Fourth ed.. Switzerland: Trans Tech Publications; 1998.
[4] Khalfaoui W, Valerio E, Masse JE, Autric M. Excimer laser treatment of ZE41 magnesium alloy for corrosion resistance and microhardness improvement. Opt Laser Eng 2010;48:926–31.
[5] Osório WR, Cheung N, Spinelli JE, Cruz KS, Garcia A. Microstructural modification by laser surface remelting and its effect on the corrosion resistance of an Al–9 wt%Si casting alloy. Appl Surf Sci 2008;254:2763–70.
[6] Cannillo V, Sola A, Barletta M, Gisario A. Surface modification of Al–Al_2O_3 composites by laser treatment. Opt Laser Eng 2010;48:1266–77.
[7] Saleh AF, Abboud JH, Benyounis KY. Surface carburizing of Ti–6Al–4V alloy by laser melting. Opt Laser Eng 2010;48:257–67.
[8] Cheung N, Pinto MA, Ierardi MCF, Garcia A. Numerical and experimental analysis of laser surface remelting of Al–15Cu alloy samples. Surf Eng 2005;21:473–9.
[9] Yilbas BS, Shuja SZ, Khan SMA, Aleem A. Laser melting of carbide tool surface: model and experimental studies. Appl Surf Sci 2009;255:9396–403.
[10] Krishnan S, Murthy JY, Garimella SV. Analysis of solid–liquid phase change under pulse heating. J Heat Transfer 2007;129:395–9.
[11] Raj PM, Sarkar S, Chakraborty S, Dutta P. Three-dimensional computational-modeling of momentum, heat and mass transfer in a laser surface alloying process. Numer Heat Transfer A 2002;42:307–26.
[12] Shen ZH, Zhang SY, Lu J, Ni XW. Mathematical modeling of laser induced heating and melting in solids. Opt Laser Technol 2001;33:533–7.
[13] Allen CM, O'Reilly KAQ, Cantor B, Evans PV. Intermetallic phase selection in 1XXX Al alloys. Prog Mater Sci 1998;43:89–170.
[14] Gremaud M, Carrard M, Kurz W. The microstructure of rapidly solidified Al–Fe alloys subjected to laser surface treatment. Acta Metall Mater 1990;38:2587–99.
[15] Griger A, Stefaniay V, Kovacs-Csetenyi E, Turmezey T. Formation and transformation of binary intermetallic phases in high purity Al–Fe alloys. Key Eng Mater 1990;44–45:17–30.
[16] Goulart PR, Lazarine VB, Leal CV, Spinelli JE, Cheung N, Garcia A. Investigation of intermetalics in hypoeutectic Al–Fe alloys by dissolution of the Al matrix. Intermetallics 2009;17:753–61.
[17] Goulart PR, Spinelli JE, Cheung N, Garcia A. The effects of cell spacing and distribution of intermetallic fibers on the mechanical properties of hypoeutectic Al–Fe alloys. Mater Chem Phys 2010;119:272–8.
[18] Incropera FP, Dewitt DP. Fundamentals of heat and mass transfer. New York: John Wiley & Sons; 1990.
[19] Hsu SC, Kou S, Mehrabian R. Rapid melting and solidification of surface due to stationary heat flux. Metall Trans 1980;11B:29–38.
[20] Steen WM. Laser material processing. London: Springer-Verlag; 2003.
[21] Ujihara K. Reflectivity of metals at high temperatures. J Appl Phys 1972;43:2376–83.
[22] Allen CM, Kumar S, Carrol L, O'Reilly KAQ, Cama H. Electron beam surface melting of model 1200 Al alloys. Mater Sci Eng A 2001;304–306:604–7.
[23] Goulart PR, Cruz KS, Spinelli JE, Ferreira IL, Cheung N, Garcia A. Cellular growth during transient directional solidification of hypoeutectic Al–Fe alloys. J Alloys Compd 2009;470:589–99.
[24] Simensen CJ, Fartum P, Andersen A. Analysis of intermetallic particles in aluminium by dissolution of the sample in butanol. Fresenius Z Anal Chem 1984;319:286–92.
[25] Gilgien P, Zryd A, Kurz W. Microstructure selection maps for Al–Fe alloys. Acta Metall Mater 1995;43:3477–87.
[26] Zhu YH, Man HC, Lee WB. Microstructure of laser melted Zn–Al based alloy. J Mater Proc Technol 2003;139:296–301.
[27] Aliravci CA, Pekguleryuz MO. Calculation of phase diagrams for the metastable Al–Fe phases forming in direct-chill (DC)-cast aluminum alloy ingots. Calphad 1998;22:147–55.
[28] Krishna BV, Bandyopadhyay A. Surface modification of AISI 410 stainless steel using laser engineered net shaping (LENS). Mater Des 2009;30:1490–6.
[29] Osório WR, Peixoto LC, Goulart PR, Garcia A. Electrochemical corrosion parameters of as-cast Al–Fe alloys in a NaCl solution. Corros Sci 2010;52:2979–93.